Journal of the Meteorological Society of Japan

**EARLY ONLINE RELEASE**



The DOI for this manuscript is
DOI:10.2151/jmsj.2022-005
J-STAGE Advance published date: October 4th, 2021

# Propagation of Convective Systems Associated with Early Morning Precipitation and Different Northerly Background Winds over Western Java

**Erma YULIHASTIN**
Research Center of Atmospheric Science and Technology, Research Organization of Aeronautics and Space, National Agency of Research and Innovation, Bandung, Indonesia

**Tri Wahyu HADI, Muhammad Rais ABDILLAH, Irineu Rakhmah FAUZIAH**
Atmospheric Sciences Research Group, Faculty of Earth Sciences and Technology, Bandung Institute of Technology, Bandung, Indonesia

and

**Nining Sari NINGSIH**
Oceanography Research Group, Faculty of Earth Sciences and Technology, Bandung Institute of Technology, Indonesia

Version: September, 2021

------------------------------------

1) Corresponding author: Erma Yulihastin, Research Center of Atmospheric Science and Technology, Research Organization of Aeronautics and Space, National Agency of Research and Innovation, Jl. Djunjunan 133, Bandung, West Java, 40173, INDONESIA.
Email: erma.yulihastin@lapan.go.id
Tel: +62-22-603-7445
Fax: +62-22-603-7443

**Abstract**

Early morning precipitation (EMP) events occur most frequently during January and February over the northern coast of West Java and are characterized by propagating systems originating from both inland and offshore. The initial location, direction, and speed of the propagating precipitating system determine the timing of EMP. This study explores processes that characterize such propagating precipitation systems by performing composite analysis and real-case numerical simulations of selected events using the Weather and Research Forecasting (WRF) model with a cloud-permitting horizontal resolution of 3 km. In the composite analysis, EMP events are classified according to the strength of the northerly background wind ($V_{BG}$), defined as the 925-hPa meridional wind averaged over an area covering western Java and the adjacent sea. We find that under both strong northerly (SN) and weak northerly (WN) wind conditions, EMP is mainly induced by a precipitation system that propagates from sea to land. For WN cases, however, precipitating systems that propagate from inland areas to the sea also play a role. The WRF simulations suggest that mechanisms akin to cold pool propagation and advection by prevailing winds are responsible for the propagating convection that induces EMP, which also explains the dependence of EMP frequency on the strength of $V_{BG}$. Based on the WRF simulations, we also discuss the roles of sea breeze and gravity waves in the initiation of convection.

**Keywords** diurnal cycle; early morning precipitation; western Java; coastal precipitation; cross-

equatorial northerly surge.

## 1. Introduction

Diurnal convection over the Maritime Continent (MC) leads to a dominant pattern in which precipitation peaks during the afternoon and night over land, and during the night and morning over sea (e.g., Qian et al. 2008). However, there are greater variations in the timing of peak precipitation over coastal regions due to propagating convective systems (Yulihastin et al. 2020). A more detailed understanding of these propagating convective precipitation systems is important, as the MC is the region with the highest coastline density (defined as coastal length divided by land area) on Earth and it receives twice as much rainfall as the global mean (Yamanaka et al. 2018).

The land–sea contrast of diurnal precipitation has mainly been explained by land–sea breeze interactions and prevailing monsoon circulations (Houze 1981), but other mechanisms are required to explain the characteristics of propagating precipitation systems (e.g., Mori et al. 2004). The key dynamic processes of such systems are likely related to the mean wind interacting with the land, producing different flow regimes; e.g., sea breezes and topographic waves. Variations in the prevailing winds can also change the rainfall and mesoscale flows over small islands (Wang and Sobel 2017).

Yulihastin et al. (2020) reported that the occurrence of early morning precipitation (EMP) events over the northern coast of West Java is strongly characterized by both land- and seaward propagating precipitation systems. Moreover, the timing of EMP events seems to be independent of the phases of land–sea breeze development. In any case, the timing of EMP events should be largely determined by two factors: (i) the location of the initial convection; and (ii) the direction and speed of propagation. To understand the possible physical processes related to these key factors, a numerical study is the most feasible approach, as detailed observations of such events are not available.

A numerical study by Wei et al. (2020) showed that the initiation of convection in the MC is associated with convergence owing to the interactions between prevailing background flows and more locally induced circulations. Their results also imply that gravity waves play an important role in determining the location of new convective systems that sustain the diurnal cycle of precipitation over the MC. Ruppert and Zhang (2019) pointed out that traveling gravity waves can potentially affect convection over a long distance across the MC. However, none of these studies examined EMP events over coastal regions.

In this study, we aim to investigate the factors associated with the development of EMP events over the northern coast of West Java by conducting real-case simulations. Based on the results of Li et al. (2017), it is expected that the propagation of coastal convection systems is mainly attributable to the effects of background winds. Several EMP events were identified by Yulihastin et al. (2020) and were found to generally coincide with the occurrence of a cross-equatorial northerly surge (CENS; Hattori et al. 2011) and the South China Sea cold tongue (SCS-CT; Koseki et al. 2013; Mori et al. 2018) in January and February. While we still consider such phenomenological attribution, this study is more focused on how EMP over western Java is influences by the strength of northerly background winds.

## 2. Data and methods

The methodology employed in this study consists of two main parts. First, we perform a composite analysis of satellite-derived precipitation data to confirm that the strength of northerly background winds can be used to distinguish different propagation characteristics of coastal precipitation. We then conduct numerical experiments on selected cases to understand the relevant physical and dynamical processes.

### 2.1 Classification and composite analysis of the effects of background wind

To investigate the effects of background wind on the propagation of convective systems from observational data, we perform a composite analysis using a TRMM Multi-Satellite Precipitation Analysis (TMPA) Real-Time 3B41RT (hereinafter TMPA-RT) dataset and the JRA-55 reanalysis dataset. TMPA-RT data consist of estimated precipitation from microwave and infrared sensors that have been calibrated using rainfall gauge data (Huffman et al. 2007). These data have been used extensively to study diurnal rainfall propagation over various regions (Harris et al. 2007; Liu et al. 2008; Yong et al. 2015), including the MC (Hassim et al. 2016; Yulihastin et al. 2020). The JRA-55 reanalysis data are used here instead of those from NCEP/NCAR because of their higher horizontal resolution. A detailed description of the JRA-55 reanalysis can be found in Kobayashi et al. (2015). We obtained the data from the Japan Meteorological Agency data portal (https://jra.kishou.go.jp/JRA-55/index_en.html).

In this study, we use samples of EMP events that were identified by Yulihastin et al. (2020). The occurrence of EMP is strongly correlated with CENS events in January and February. Hence, we categorize the EMP events according to the strength of the prevailing northerly background wind, $V_{BG}$, which is defined as the 925-hPa meridional wind velocity averaged over the rectangular area 105.5°E–108.5°E, 3°S–7.5°S (red boxes in Fig. 1). We categorize the northerly background wind into two groups:

- Strong northerly (SN): $V_{BG} \leq V_M$,
- Weak northerly (WN): $V_M < V_{BG} \leq 0$,

where $V_M = -6.3\ \mathrm{m\ s^{-1}}$ is the median value calculated for all EMP events.

Table 1 lists the dates of EMP events falling into each of the two categories. From a total of 50 EMP events, we obtained 24 SN samples, 23 WN samples, and 3 samples that do not fall into either SN or WN categories because $V_{BG}$ > 0 (Fig. S1). These three rare events are regarded as outliers and are excluded from the composites; however, one of the three events is numerically simulated and the results are discussed in the context of the initiation of inland convection (see Section 5). Composite maps of wind fields and 24-hour time–latitude Hovmöller diagrams for the SN and WN cases are plotted in Fig. 2.

## 2.2 Numerical simulation using the WRF model

To understand the dynamical factors that affect the propagation of precipitation systems towards the coastal region, we perform a numerical simulation of two EMP events representing each of the two EMP categories. The events of 8–9 February 2008 (Case 1) and 4–5 January 2005 (Case 2) are selected as the SN and WN cases, respectively. They were manually selected after inspecting the results of several attempted simulations. Due to limited computational resources, we could only conduct case studies rather than simulating all EMP events.

We used the Weather Research and Forecasting (WRF) model version 3.9.1.1 (Skamarock et al. 2008). The initial and boundary conditions were derived from the National Center for Environmental Prediction Final Analysis (NCEP–FNL) and have a spatial and temporal resolution of 1° and 6 hours, respectively. Table 2 shows the WRF model configuration, which was adopted from Fonseca et al. (2015) who succeeded in simulating diurnal precipitation over the MC and capturing offshore propagation over the coastal region. The results are in good agreement with satellite-observed precipitation in terms of intensity, duration, timing, and location (Yulihastin et al. 2021). However, to ensure that the WRF model can realistically simulate the EMP events, we perform sensitivity tests with convective parameterization, 3 model domains, and spin-up. The sensitivity tests showed that a better representation of EMP events is obtained by using three nested domains (Fig. 1) with Betts–Miller–Janjić (BMJ) convective parameterization (Janjić, 1994) and a 24-hour spin-up time. In the third domain, the horizontal resolution is 3 km, allowing shallow convection to be explicitly resolved. Other model parameters are from Fonseca et al. (2015) except for the Planetary Boundary Layer scheme, for which we use the WRF default settings (see Table 2).

## 3. Composite analysis of early morning precipitation events under different northerly background winds

Figure 2 shows composite maps and Hovmöller diagrams for EMP events that are classified into the SN and WN categories. The synoptic pattern of the 925-hPa wind field indicates a meridional flow that is predominantly northerly, suggesting the influence of the Asian winter monsoon during the study period. However, stronger northerly winds are observed over the regions extending southward from the SCS to the north of western Java (Fig. 2a, d). Moreover, the composite maps in Fig. 2b, e indicate that precipitation is more strongly concentrated over the coastal region under SN conditions than under WN conditions.

In Hovmöller diagrams, the early morning peaks in precipitation over the northern coast of West Java are well captured in both cases (Fig. 2c, f). The main differences in the characteristics of the propagation and extent of EMP between the two composites are as follows.

- The SN group shows a more confined EMP signal with a seaward extension to approximately 4.5°S in the Java Sea (Fig. 2b) and a more prominent sea-to-land (hereinafter $\beta$) propagation pattern. The SN composite is also characterized by signals of earlier precipitation events that occurred in the late afternoon, between 19:00 LST and 22:00 LST.
- The WN group also shows a $\beta$ propagation pattern that extends north of 4°S (Fig. 2e). In addition, afternoon precipitation occurs deeper inland, peaking at around 19:00 LST and followed by a land-to-sea (hereinafter $\alpha$) propagation pattern.

Figure 2 clearly shows the strong effects of northerly background winds on the onshore-propagating precipitation, leading to EMP events over the northern coast of West Java. The contrasting effects of southerly background winds can be seen in the rare outlier events where $V_{BG}$ > 0, which are dominated by seaward-propagating precipitation (Fig. S1).

Most of the EMP events coincide with enhanced northerlies associated with CENS (Yulihastin et al. 2020). In the SN cases, the strengthening of northerlies over the northern SCS may be modulated by cold surge episodes (Lim et al. 2017). This could then promote the CENS and eventually enhance precipitation over Java Island (Hattori et al. 2011). Increased moisture fluxes toward the MC during cold surge periods (Abdillah et al. 2021) may also influence the development of night-time convection over the sea that is shifted towards land (Koseki et al. 2013). However, the WN cases indicate that enhanced coastal precipitation and EMP events may also occur without CENS. In summary, both SN and WN cases are characterized by propagating precipitation systems that are connected to EMP.

## 4. Simulated Propagating Convection over Land and the Java Sea

We conducted numerical simulations of the two selected EMP events to further understand the processes that control the propagating coastal precipitation (see Section 2.2). Observed features of the two EMP events are depicted in Fig. 3, with time-snapshot maps and Hovmöller diagrams showing the evolution of precipitation systems corresponding to the events. Different snapshots are plotted to illustrate the features that are most relevant to each case. The EMP event of Case 1 is characterized by concentrated precipitation along the coastal regions of western Java (Fig. 3a-c) with pronounced $\beta$ propagation (Fig. 3d), which is consistent with the SN composite shown in Fig. 2c. In contrast, the WN of Case 2 exhibits more complex features, with precipitating systems originating from regions both north and south of the coastline. A $\beta$ propagation pattern is evident (Fig. 3h), and although α propagation cannot be clearly identified, a relatively large region of precipitation appeared from 23:00 LST on 4 January 2005 and persisted until the next morning over the southwest of the study area.

Results from the numerical simulation of the two selected cases are shown in Fig. 4. By comparing Fig. 4 and Fig. 3, we can see that the $\beta$ propagation patterns in the observed and simulated features are in qualitative agreement, while there are some discrepancies in the timing and exact location of the peak precipitation. Considering that the model was not fine-tuned to match observations, these simulations should still be appropriate for investigating the mechanisms responsible for the propagation of convective systems approaching the coastline from offshore. The initiation of both inland and offshore convection is another key factor in understanding EMP, and is addressed separately in Section 5 owing to there being fewer supporting data to confirm the model results.

Figure 5 shows the simulated propagating precipitating systems in Case 1 (EMP under SN conditions). At 00:00 LST, there are two precipitation centers near points A (offshore) and B (near the coastline). From 01:00 LST to 05:00 LST, the convective activities around point B are characterized by rapidly developing and decaying clouds, with high values of $\theta_e$ below the 1 km level. The cloud systems slowly migrate to the northeast over time. The propagation of offshore convection to the coastline along the A–B transect is clearly simulated.

The convection near point A develops by 00:00 LST, but then moves and decays quite rapidly around 200 km from the coastline by 01:00 LST. This is when a $\theta_e$ anomaly, which we interpret as a “cold pool” (CP), starts to develop below 0.5 km altitude. At 02:00 LST, the CP moves closer to the coastline to about 150 km offshore and seems to induce deep convection leeward. Interestingly, another deep convective cell develops windward of the cold pool, resembling a “back-building” mechanism in a mesoscale convective system (MCS). This mechanism is a quasi-stationary system that forms as a result of lifting generated by cold pools inside the MCS structure (Schumacher and Johnson 2005; Yulihastin et al. 2021).

Although there is almost no precipitation over land in the simulated EMP event for Case 1, these results suggest that the observed propagating precipitation systems associated with EMP events can be explained by cold pool development below a decaying convective cloud and its advection by the prevailing background wind. This mechanism also explains the preferred direction of propagation; i.e., from land to sea in the event of northerly winds, and vice versa in the event of southerly winds. Thus, $\beta$ propagation of precipitation systems occurs more frequently under SN conditions that are influenced by CENS (Yulihastin et al. 2020), which is also in agreement with the results of Koseki et al. (2013).

For the Case 1 simulation, we can roughly estimate the speed of onshore CP propagation from Fig. 5 by tracing the movement of the leading edge of the CP along the path of the A–B transect, yielding a figure of around 12 $\mathrm{m\,s^{-1}}$. This propagation speed is somewhat slower than that of gravity waves, which is between about 15 $\mathrm{m\,s^{-1}}$ (Mapes et al. 2003) and 17 $\mathrm{m\,s^{-1}}$ (Ruppert and Zhang 2019), but nevertheless the two may still be related.

It is necessary to examine the consistency of the model results. If a CP behaves like a density current, its propagation speed should be proportional to the depth of the CP and the density difference between the CP and the ambient air. Under the influence of background winds and vertical wind shear, the propagation speed of a CP can exceed 10 $\mathrm{m\,s^{-1}}$ (Hutson et al. 2019). If the CP mechanism holds for most cases, a slower propagation speed (Schlemmer and Hohenegger 2016) should be observed under weaker background winds and over land where surface roughness could also affect air movement.

As mentioned above, Case 2 is an example of an EMP event belonging to the WN category (Table 1). Figure 4 shows that the horizontal winds over Java in Case 2 are not weaker than in Case 1, but the northerly winds inland are suppressed owing to counteracting southerlies. As a result, there seem to be multiple EMP events with both $\alpha$ and $\beta$ propagation occurring over the northern coast of West Java. Despite an overall complex situation, we can see the clear evolution of convective cells in Fig. 6. Deep convection appears at 20:00 LST and decays at 21:00 LST, inducing a CP that spreads over several kilometers. Like Case 1, the CP is advected towards the coastline, but without inducing new convection, until it penetrates deeper to about 25 km onshore. We estimate that the propagation speed of the CP is around 7 $\mathrm{m\,s^{-1}}$, which is slower than that of Case 1 (offshore propagation under SN conditions).

Our results from the WRF simulation confirm that CP propagation and advection by background winds is a plausible mechanism for the propagating convective systems associated with EMP events over the northern coast of West Java. The direction of propagating convective systems relative to the coastline is determined by the prevailing background wind, in agreement with Li et al. (2017). Although our model resolution is still too coarse to simulate the detailed structure of the CP, the propagation speed (7 to 12 $\mathrm{m\,s^{-1}}$) is comparable to that of observed precipitation from TMPA data (Fig. 4). This implies that once a CP has been generated below a decaying precipitation system, it can serve as a self-replicating mechanism (Mori et al. 2004) for more convection, both offshore and onshore, with various propagation speeds. Moreover, because the propagation of the CP is not necessarily phase-locked to the land–sea breeze, the timing of the CP-induced precipitation peak is somewhat random (Yulihastin et al. 2020). However, the timing and location of the first convective system, with a scale that can generate a CP, may be influenced by the land–sea breeze and gravity waves (e.g., Wei et al. 2020). Therefore, we briefly discuss this matter in the following section.

## 5. Discussion

We have shown from satellite observations and numerical simulations that the propagation of convective systems over the sea is a key process in inducing EMP over the northern coast of West Java. The initial location and timing of the developing convection are also important, but their identification from satellite and reanalysis data is more difficult. Therefore, we discuss these key aspects using the WRF simulations.

The most well-understood mechanism that can initiate diurnal convection is sea breeze convergence (e.g., Yang and Slingo 2001). In this study, the role of sea breeze in the initiation of convection is best illustrated by simulating the case of 19 January 2012, which is one of the three outlier EMP events (hereinafter referred to as Case 3). Figure 7 shows the observed and simulated precipitation for this case, where the daily averaged 925-hPa reanalysis wind field (Fig. 7a–c) is characterized by southerlies. On the other hand, the simulated 10 m wind fields in Fig. 7e–g show large temporal variations, indicating the strong influence of a sea breeze from 14:00 LST to 18:00 LST.

The role of sea breeze in the initiation of inland convection should be clearly evident for Case 3 because it is the only conceivable major factor coming from the sea without any precipitating system before 18:00 LST. Similarly to Fig. 7, Fig. 8 shows the spatial–temporal evolution of convective activity, but with the wind anomaly vectors computed as the departure from the daily mean, whereby the sea-breeze signature can be identified as an enhanced onshore flow at 16:00 LST and 18:00 LST. At 16:00 LST the atmospheric flow over land is characterized by eddy-like structures without significant cloud development; however, convection appears to strengthen further south of the mountainous region, which matures later at 18:00 LST. Of note, the depth of the sea-breeze flow generated in the WRF model is ~1 km, which is comparable to observations (Hadi et al. 2000), and its role in initiating convection deeper inland is quite clear.

In addition to the initiation of convection, the simulated Case 3 also demonstrates that it is possible for an EMP event to be induced solely by a land-to-sea or *α* propagation pattern. We analyzed the simulated convective propagation in Case 3 (Fig. S2), which did not occur until after the sea-breeze flow had ceased at 20:00 LST. We found that the *α* propagation of the convection also involves CP propagation and advection, as in Cases 1 and 2. The estimated propagation speed of the CP for Case 3 is about 5 m $s^{-1}$. This speed means the CP could be classed as a gravity current, but it is too slow to be attributable to gravity waves. Moreover, the seaward (*α*) propagation of the convective systems is consistent with the effects of background wind.

The initiation of convection over the sea is more difficult to explain by the effects of land breeze, especially under SN conditions. Therefore, we examine the Case 1 simulation for the possible influence of gravity waves in the initiation of convection offshore around 00:00 LST (see Fig. 5). Figure 9 shows the meridional and zonal variations of temperature anomaly profiles after subtracting the diurnal cycle. Wave-like structures in the temperature profiles seem to be more prominent in the longitudinal direction at 20:00 LST. Over point X, where the initial convection in Case 1 occurs, temperature profiles become increasingly unstable below 700 hPa owing to a downward-propagating low-temperature anomaly. These layered structures of temperature anomalies become disrupted when convection occurs at 00:00 LST. This indicates the possible influence of zonally propagating gravity waves on the initiation of convection offshore of western Java, which is consistent with the results of Ruppert and Zhang (2019) and Wei et al. (2020).

## 6. Conclusion

We investigated the processes responsible for the propagating precipitation systems associated with early morning precipitation (EMP) events identified by Yulihastin et al. (2020). First, we performed a composite analysis on TMPA-RT for EMP events that were classified according to the strength of the northerly background winds. Second, we conducted numerical simulations of two selected events (one strong northerly (SN) and one weak northerly (WN) case) using the WRF model, with a configuration adopted from Fonseca et al. (2015). The main results can be summarized as follows.

- Both satellite observations and the WRF model simulations clearly indicate that the strength of the northerly background wind affects the characteristics of propagating precipitation systems offshore and onshore along the northern coasts of West Java. For SN conditions, the sea-to-land propagation pattern is dominant, while WN conditions give rise to a complex mixture of onshore and offshore patterns.

- The WRF simulations suggest that cold pools (CPs) generated below decaying convective clouds induce new convective cells near their leading and/or trailing edge while propagating and being advected by the background wind. An additional simulation showed that the CP-induced propagation is consistently reproduced for onshore convection under a weak southerly background wind. Hence, this is a plausible “self-replicating” mechanism for the propagation of precipitating systems near coastal regions in the MC, as proposed by Mori et al. (2004). Recent studies have reported that both onshore- and offshore-propagating convective systems could produce CPs (Trismidianto et al. 2016), which determine the speed of the propagation and help to maintain a long-lasting mesoscale convective complex (Yulihastin et al. 2021).

The CP mechanism is also consistent with the tendency of precipitation to accumulate closer to land during active periods of SCS-CT, in association with the more frequent occurrence of CENS (Koseki et al. 2012; Yulihastin et al. 2020). The propagation speed of the simulated CP varies from 5 $\mathrm{m\,s^{-1}}$ to 12 $\mathrm{m\,s^{-1}}$, which is reasonable considering the wide range of CP propagation speeds (Hutson et al. 2019; Yulihastin et al. 2021), and this results in a more random timing of peak precipitation during EMP events (Yulihastin et al. 2020).

The mechanisms involved in the development of initial convection that generates propagating CPs are important to understand, but they have only been discussed briefly in this work. It has been demonstrated that sea breeze and gravity waves may play important roles, as proposed in numerous other studies. However, large precipitation systems such as MCSs may also generate CP-like environments by the so-called sprinkler effect (Yamanaka et al. 2019) and trigger convection over a wider area. More studies are needed to investigate each of these mechanisms in more detail using observations. Considering that background synoptic flows are influenced by large-scale environmental conditions (Peatman et al., 2021), future studies should also explore model uncertainties associated with the multiple processes involved in the initiation and propagation of precipitating systems to improve weather prediction in the MC.

## Acknowledgments

This work was supported by the Indonesia Educational Endowment Fund (LPDP) through the Mandatory Productive Innovative Research program under National Research Priority [252/Menteri Ristek/Ka BRIN/E1/PRN/2020]. The co-authors (TWH and MRA) were partially supported by the Java Flood One research project funded by the Newton Fund NERC and the Indonesian Ministry of Education and Culture. The authors greatly thank Dr. Didi Satiadi of the National Agency of Research and Innovation, Dr. Nurjanna Joko Trilaksono and Dr.rer.nat. Mutiara Rachmat Putri of Institut Teknologi Bandung for their useful discussions and suggestions. The authors would also like to express their appreciation to Prof. Adrian Matthews of the University of East Anglia and other research team members of TerraMaris under the Years of the Maritime Continent Joint Research Program (2020-2021) for their useful comments.

## References

Abdillah, M. R., Y. Kanno, T. Iwasaki, J. Matsumoto, 2021: Cold Surge Pathways in East Asia and Their Tropical Impacts, *J. Climate*, **34**,157–170.

Fonseca, R. M., T. Zhang, and K. T. Yong, 2015: Improved Simulation of Precipitation in the Tropics using a Modified BMJ Scheme in the WRF Model, *Geosci. Model Dev.*, **8**, 2915–2928.

Hadi, T. W., T. Tsuda, H. Hashiguchi, and S. Fukao, 2000: Tropical Seabreeze Circulation with L-band, *J. Meteorol. Soc. Jpn.*, **78**, 123–140.

Harris, A., S. Rahman, F. Hossain, L. Yarborough, A. C. Bagtzoglou, and G. Easson, 2007: Satellite-based Food Modelling using TRMM-based Rainfall Products, *Sensors*, **7**, 3416–3427.

Hattori, M., S. Mori, and J. Matsumoto, 2011: The Cross-Equatorial Northerly Surge over the Maritime Continent and Relationship to Precipitation Patterns, *J. Meteorol. Soc. Jpn.*, **89**, 27–47.

Hassim, E. E., T. P. Lane, and W. W. Grabowski, 2016: The Diurnal Cycle of Rainfall over New Guinea in Convection-Permitting WRF Simulations, *Atmos. Chem. Phys.*, **16**, 161–175.

Houze, R. A., S. G. Geotis, F. D. Marks, and A. K. West, 1981: Winter Monsoon Convection in the Vicinity of North Borneo. Part I Structure and Time Variation of the Clouds and Precipitation, *Mon. Weather Rev.*, **109**, 1595–1614.

Huffman, G. J., R. F. Adler, S. Curtis, D. T. Bolvin, G. Gu, E. J. Nelkin, K. P. Bowman, Y. Hong, E. F. Stocker, and D. B. Wolf, 2007: The TRMM Multi-Satellite Precipitation Analysis (TMPA): Quasi-global, Multiyear, Combined Sensor Precipitation Estimates at Fine Scales, *J. Hydrometeorol.*, **8**, 38–55.

Hutson, A., C. Weiss, and G. Bryan, 2019: Using the Translation Speed and Vertical Structure of Gust Fronts to Infer Buoyancy Deficits within Thunderstorm Outflow, *Mon. Weather Rev.*, **147**, 3575–3594.

Janjić, Z. I., 1994: The Step-Mountain Eta Coordinate Model: Further Developments of the Convection, Viscous Sublayer and Turbulence Closure Schemes, *Mon. Weather Rev.*, **122**, 927–945.

Kobayashi, S., Y. Ota, Y. Harada, A. Ebita, M. Moriya, H. Onoda, K. Onogi, H. Kamahori, C. Kobayashi, H. Endo, K. Miyaoka, and K. Takahashi, 2015: The JRA-55 Reanalysis: General Specifications and Basic Characteristics, *J. Meteorol. Soc. Jpn.*, **93**, 5–48.

Koseki, S., T-Y. Koh, and C-K. Teo, 2013: Effects of The Cold Tongue in The South China Sea on The Monsoon, Diurnal Cycle and Rainfall in The Maritime Continent, *Q. J. R. Meteorol. Soc.*, **139**, 1566–1582.

Li, Y., N. C. Jourdain, A. S. Taschetto, A. S. Gupta, D. Argüeso, S. Masson, and W. Cai, 2017: Resolution Dependence of the Simulated Precipitation and Diurnal Cycle over the Maritime Continent, *Clim. Dynam.*, **48**, 4009–4028.

Lim, S. Y., C. Marzin, P. Xavier, C-P. Chang, and B. Timbal, 2017: Impacts of Boreal Winter Monsoon Cold Surges and the Interaction with MJO on Southeast Asia Rainfall, *J. Climatol*, **30**, 4267–4281.

Liu, C., M. W. Moncrieff, and J. D. Tuttle, 2008: A Note Propagating Rainfall Episodes over The Bay of Bengal, *Q. J. R. Meteorol. Soc.*, **134**, 787–792.

Mapes, B. E., T. T. Warner, and M. Xu, 2003: Diurnal Patterns of Rainfall in Northwestern South America. Part III Diurnal Gravity Waves and Nocturnal Convection Offshore, *Mon. Weather Rev.*, **131**, 830–844.

Mori, S., H. Jun-Ichi, I. T. Yudi, D. Y. Manabu, O. Noriko, M. Fumie, S. Namiko, H. Hiroyuki, and S. Tien, 2004: Diurnal Land–sea Rainfall Peak Migration over Sumatera Island, Indonesian Maritime Continent, Observed by TRMM Satellite and Intensive Rawinsonde Soundings, *Mon. Weather Rev.*, **132**, 2021–2039.

Mori, S., J.-I. Hamada, M. Hattori, P.-M. Wu, M. Katsumata, N. Endo, K. Ichiyanagi, H. Hashiguchi, A. A. Arbain, R. Sulistyowati, L. Sopia, F. Syamsudin, T. Manik, and M. D. Yamanaka, 2018: Meridional March of Diurnal Rainfall Over Jakarta, Indonesia, Observed With a C-band Doppler Radar an Overview of the HARIMAU2010 Campaign, *Prog. Earth Planet. Sci.*, **5**, 1–23.

Peatman, S. C., J. Schwendike, C. E. Birch, J. H. Marsham, A. J. Matthews, and G.-Y. Yang, 2021: A Local-to-Large Scale View of Maritime Continent Rainfall: Control by ENSO, MJO and Equatorial Waves, *J. Climatol.*, 1-52, doi:10.1175/JCLI-D-21-0263.1

Qian, J. H., 2008: Why Precipitation is Mostly Concentrated over Islands in the Maritime Continent, *J. Atmos. Sci.*, **65**, 1428–1441.

Ruppert, J. H., and F. Zhang, 2019: Diurnal Forcing and Phase Locking of Gravity Waves in The Maritime Continent, *J. Atmos. Sci.*, **76**, 2815–2835.

Schlemmer, L., and C. Hohenegger, 2016: Modifications of The Atmospheric Moisture Field as A Result of Cold-pool Dynamics, *Q. J. R. Meteorol. Soc.*, **142**, 30–42.

Schumacher, R. S., and R. H. Johnson, 2005: Organization and Environmental Properties of Extreme-Rain-Producing Mesoscale Convective Systems, *Mon. Weather Rev.,* **133**, 961–976.

Skamarock, W. C., J. B. Klemp, J. Dudhia, D. O. Gill, D. Barker, M. G. Duda, and J. G. Powers, 2008: A Description of the Advanced Research WRF Version 3. NCAR Technical Note No. NCAR/TN–475+STR, *University Corporation for Atmospheric Research*, doi:10.5065/D68S4MVH.

Trismidianto, T. W. H., S. Ishida, Q. Moteki, A. Manda, and S. Iizuka 2016: Development Processes of Oceanic Convective Systems Inducing the Heavy Rain over the Western Coast of Sumatra on 28 October 2007, *SOLA*, **12**, 6–11.

Wang, S., and A. H. Sobel, 2017: Factors Controlling Rain on Small Tropical Islands: Diurnal Cycle, Large-Scale Wind Speed, and Topography, *J. Atmos Sci.*, **74**, 3515–3532.

Wei, Y., Z. Pu, and C. Zhang, 2020: Diurnal Cycle of Precipitation over the Maritime Continent Under Modulation of MJO: Perspectives from Cloud-permitting Scale Simulations, *J. Geophys. Res.: Atmos.*, **125**, 1–38.

Yamanaka, M. D., S.-Y. Ogino, P.-M. Wu, J.-I. Hamada, S. Mori, J. Matsumoto, and F. Syamsudin, 2018: Maritime Continent Coastlines Controlling Earth's Climate, *Progress in Earth and Planetary Science*, **5**, 1–28.

Yang, G-Y., and J. Slingo, 2001: The Diurnal Cycle in the Tropics, *Mon. Weather Rev.*, **129**, 784–801.

Yong, B., D. Liu, J. J. Gourley, Y. Tian, G. J. Huffman, L. Ren, and Y. Hong, 2015: Global View of Real-Time TRMM Multisatellite Precipitation Analysis, *BAMS*, **96**, 283–296.

Yulihastin, E., T. W. Hadi, N. S. Ningsih, and M. R. Syahputra, 2020: Early Morning Peaks in the Diurnal Cycle of Precipitation over The Northern Coast of West Java and Possible Influencing Factors, *Ann. Geophys.*, **38**, 231–242.

Yulihastin, E., I. Fathrio, Trismidianto, F. Nauval, E. Saufina, W. Harjupa, D. Satiadi, and D. E. Nuryanto, 2021: Convective Cold Pool Associated with Offshore Propagation of Convection System over the East Coast of Southern Sumatra, Indonesia, *Adv. Meteorol.,* 1-13, https://doi.org/10.1155/2021/2047609.

## List of Figures

Fig. 1 Figure 1. Configuration of model domains for simulating precipitation systems over the Maritime Continent. The first (D01), second (D02), and third (D03) domain have horizontal resolutions of 27 km, 9 km, and 3 km, respectively.

Fig. 2 Composite averages of EMP events classified as (a–c) strong northerly and (d–f) weak northerly cases (Table 1). (a, d) Daily mean of the 925-hPa wind field (color shading for the meridional component). Red boxes (105.5°E–108.5°E, 3°S–7.5°S) indicate the spatial window for measuring the background wind strength. (b, e) EMP rates averaged over 01:00–05:00 LST. (c, f) Hovmöller diagrams of diurnal precipitation in local time. The black dashed lines mark the northern coastline of western Java. Hatched areas indicate regions where differences between SN and WN composites satisfy statistical significance test (90% confidence levels). Black arrows denote land-to-sea (α) and sea-to-land (β) propagating systems.

Fig. 3 Temporal evolution of 925-hPa winds (vectors) and precipitation (shading) during the EMP events on (a–d) 8–9 February 2008 (Case 1) and (e–h) 4–5 January 2005 (Case 2), representing the strong northerly and weak northerly cases, respectively. (a–c) and (e–g) show full spatial structures that are averaged over the hours noted in local time at the top of the panels (hours). The Hovmöller diagrams in (d) and (h) show propagating precipitation associated with EMP events; black arrows denote land-to-sea (β) propagating systems of interest.

Fig. 4 Same as Fig. 3, but for the WRF model simulations. The simulated wind is at 10 m. Black arrows in (d) and (h) are the simulated land-to-sea (β) propagating systems that are comparable with the observed propagating systems in Fig. 3.

Fig. 5 Time evolution of Case 1 from 00:00–05:00 LST. (a–f) Spatial pattern of hourly precipitation (shading) and 10-m horizontal winds (vectors); (g–l) vertical cross sections of winds (vectors; vertical component multiplied by 40), equivalent potential temperature (contours), and cloud mixing ratio (shading) along the thick black line from point A to point B shown in panels (a–f). The x-axis is the distance in km from point X shown in panels (a–f). For clarity, the equivalent potential temperature has had 343 K subtracted from it. Blue (red) lines indicate negative (positive) values, with a contour interval of 1.5 K starting from −0.5 K (0.5 K).

Fig. 6 Same as Fig. 5, but for Case 2.

Fig. 7 (a–d) Observed and (e–h) simulated features of a unique EMP event that occurred on 19 January 2012 (Case 3). Panels (a–c) and (e–g) show full spatial structures that have been averaged over the hours shown in local time at the top of the panels. Panels (d) and (h) show Hovmöller diagrams of precipitation based on the red box shown in Fig. 2. Shading denotes the rain rate. Vectors denote (a–c) the background wind field at 925 hPa and (e–g) the hourly wind field at 10 m.

Fig. 8. As in Fig. 5, but for Case 3. Spatial pattern of precipitation at: (a) 16:00 LST, (b) 18:00 LST, (c) 20:00 LST; and vertical cross sections along the thick black line from point A to point B of winds (vectors; vertical component multiplied by 40), equivalent potential temperature (contours), and cloud mixing ratio (shading) at: (d) 16:00 LST, (e) 18:00 LST, and (f) 20:00 LST.

Fig. 9. Vertical cross sections of potential temperature anomalies in Case 1 along (a–f) line A over 19:00–00:00 LST, and (g–l) line B over 19:00–00:00 LST. Pressure levels are given in hPa. The anomalies are constructed by subtracting the first harmonic of the diurnal cycle. Regions for lines A and B are shown in top left-hand corner.

## List of Tables

Table 1. List of early morning precipitation (EMP) events that are classified into two main groups and an outlier group based on the background wind. The parameter $V_{BG}$ is the 925-hPa meridional wind averaged over 105.5°E–108.5°E, 3°S–7.5°S (see Fig. 2). Events selected for our modelling study are printed in bold.

| **Group** | **Criteria** | **Identified Cases** | **# of Cases** |
|---|---|---|---|
| Strong northerlies (SN) | $V_{BG} < -6.3\ m/s$ | 10Feb2001, 01Feb2002, 03Feb2002, 04Feb2002, 10Feb2002, 12Feb2002, 13Feb2002, 16Feb2002, 26Jan2006, 27Jan2006, 28Jan2006, 27Feb2006, 01Jan2008, **08Feb2008**, 13Feb2008, 14Feb2008, 18Feb2008, 13Jan2009, 14Jan2013, 17Jan2014, 18Jan2014, 20Jan2014, 02Feb2014 | 23 |
| Weak northerlies (WN) | $-6.3\ m/s < V_{BG} \leq 0$ | 28Jan2003, 03Jan2004, **04Jan2005**, 07Feb2005, 28Jan2007, 02Feb2008, 04Feb2008, 05Feb2008, 31Jan2009, 09Feb2009, 14Jan2010, 22Feb2010, 05Jan2013, 20Feb2013, 21Feb2013, 22Feb2013, 12Jan2014, 01Feb2014, 03Feb2014, 18Feb2014, 22Jan2016, 29Jan2016, 03Feb2016, 21Feb2016 | 24 |
| Outliers | $V_{BG} > 0$ | 07Jan2002, **19Jan2012**, 03Jan2014 | 3 |
| **Total** | | | 50 |

Table. 2 Model configuration (adopted from Fonseca et al. 2015) used in this study for the simulation of real EMP events (see Fig. 1 for the spatial domain configuration).

| **Parameterization** | **Betts–Miller– Janji´c (BMJ) Scheme** | | |
|---|---|---|---|
| | D01 (27km) | D02 (9km) | D03 (3km) |
| **Cumulus** | BMJ | BMJ | - |
| **Microphysics** | WDM5 | WDM5 | WDM5 |
| **PBL** | MYJ | MYJ | MYJ |
| **SW-Radiation** | RRTMG | RRTMG | RRTMG |
| **LW-Radiation** | RRTMG | RRTMG | RRTMG |
| **Surface Layer** | Monin-Obukhov | Monin-Obukhov | Monin-Obukhov |
| **Land Surface** | 4-layer Noah LS | 4-layer Noah LS | 4-layer Noah LS |

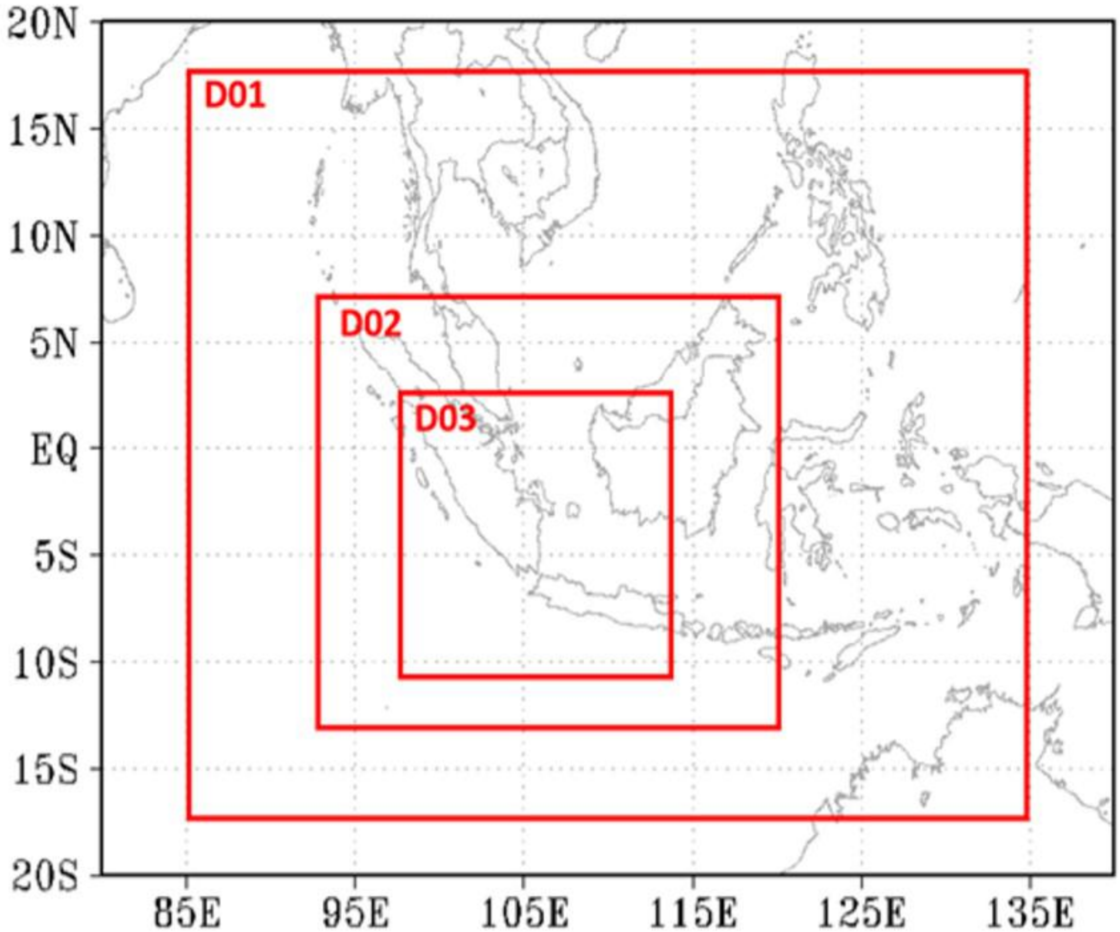


Figure 1. Configuration of model domains for simulating precipitation systems over the Maritime Continent. The first (D01), second (D02), and third (D03) domain have horizontal resolutions of 27 km, 9 km, and 3 km, respectively.

154x120mm (96 x 96 DPI)

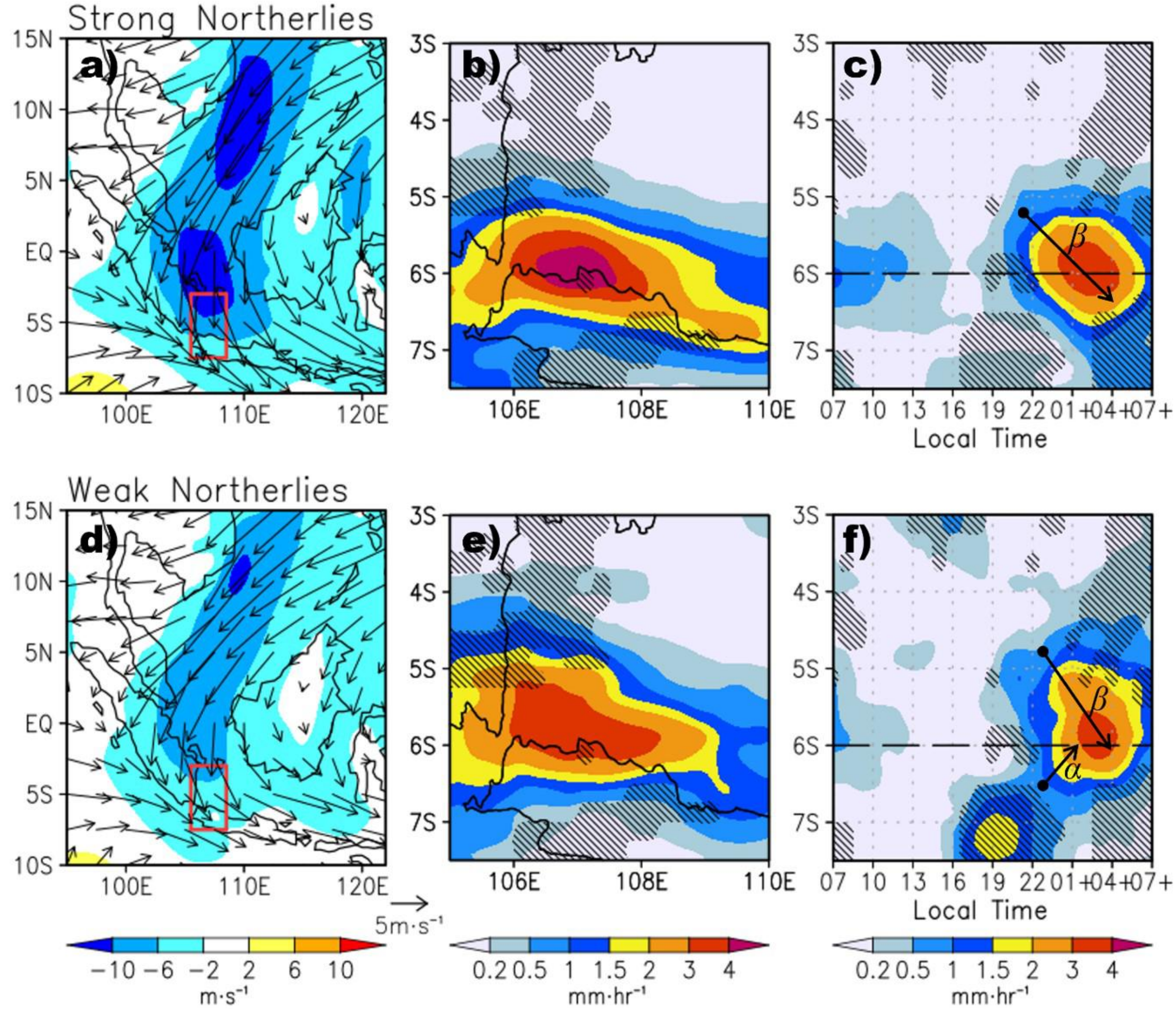


Figure 2. Composite averages of EMP events classified as (a–c) strong northerly and (d–f) weak northerly cases (Table 1). (a, d) Daily mean of the 925-hPa wind field (color shading for the meridional component). Red boxes (105.5°E–108.5°E, 3°S–7.5°S) indicate the spatial window for measuring the background wind strength. (b, e) EMP rates averaged over 01:00–05:00 LST. (c, f) Hovmöller diagrams of diurnal precipitation in local time. The black dashed lines mark the northern coastline of western Java. Hatched areas indicate regions where differences between SN and WN composites satisfy statistical significance test (90% confidence levels). Black arrows denote land-to-sea (α) and sea-to-land (β) propagating systems.

170x143mm (150 x 150 DPI)

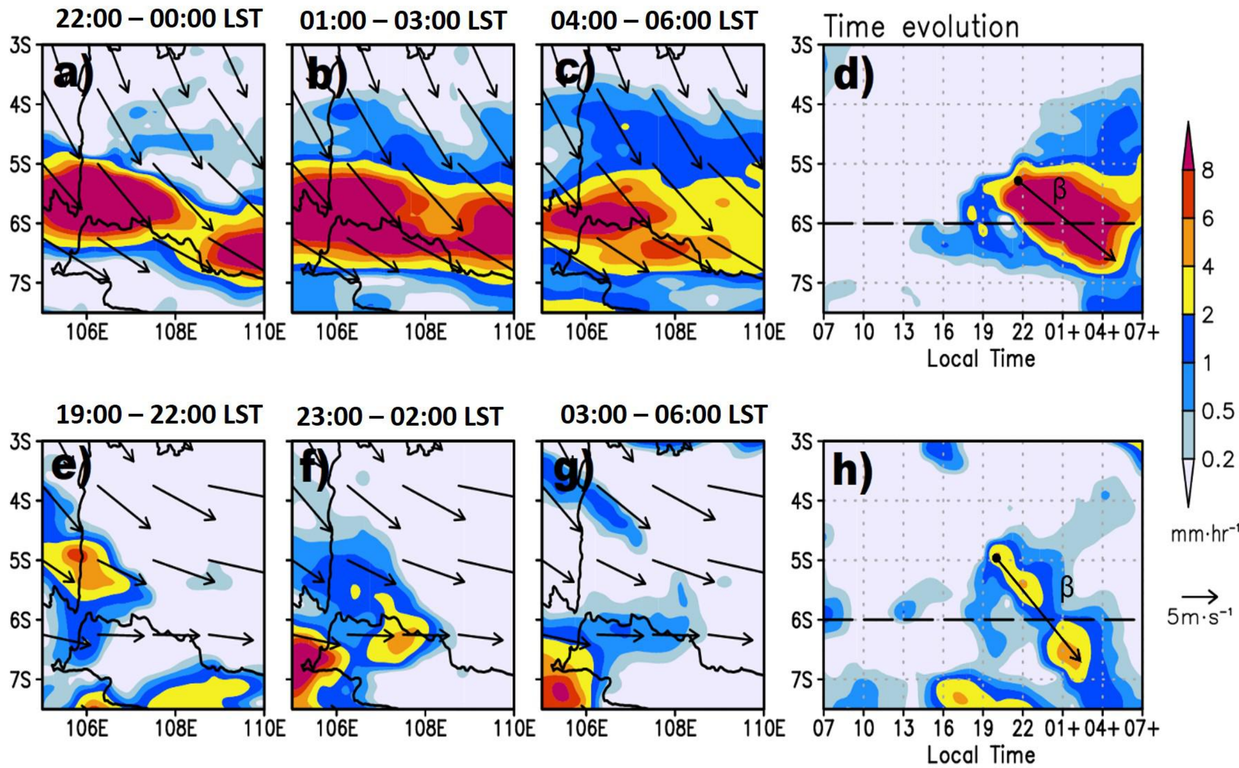


Figure 3 Temporal evolution of 925-hPa winds (vectors) and precipitation (shading) during the EMP events on (a–d) 8–9 February 2008 (Case 1) and (e–h) 4–5 January 2005 (Case 2), representing the strong northerly and weak northerly cases, respectively. (a–c) and (e–g) show full spatial structures that are averaged over the hours noted in local time at the top of the panels (hours). The Hovmöller diagrams in (d) and (h) show propagating precipitation associated with EMP events; black arrows denote land-to-sea (β) propagating systems of interest.

170x96mm (150 x 150 DPI)

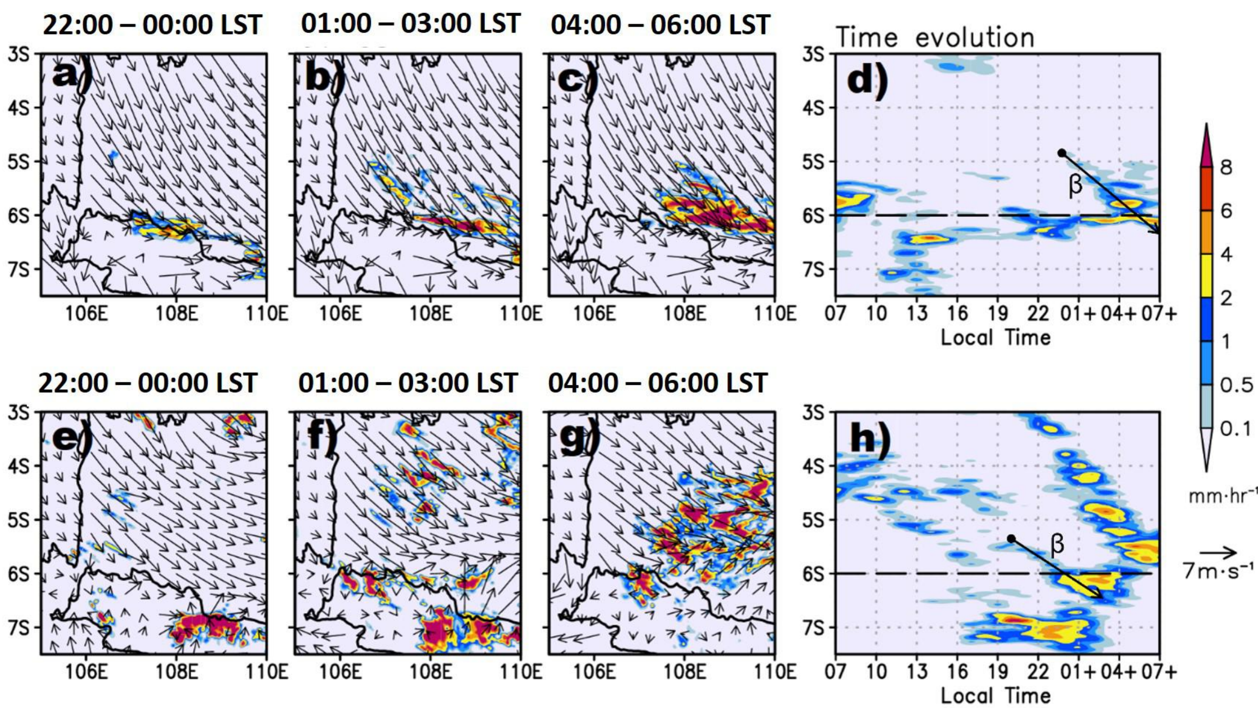


Figure 4. Same as Fig. 3, but for the WRF model simulations. The simulated wind is at 10 m. Black arrows in (d) and (h) are the simulated land-to-sea (β) propagating systems that are comparable with the observed propagating systems in Fig. 3.

170x96mm (150 x 150 DPI)

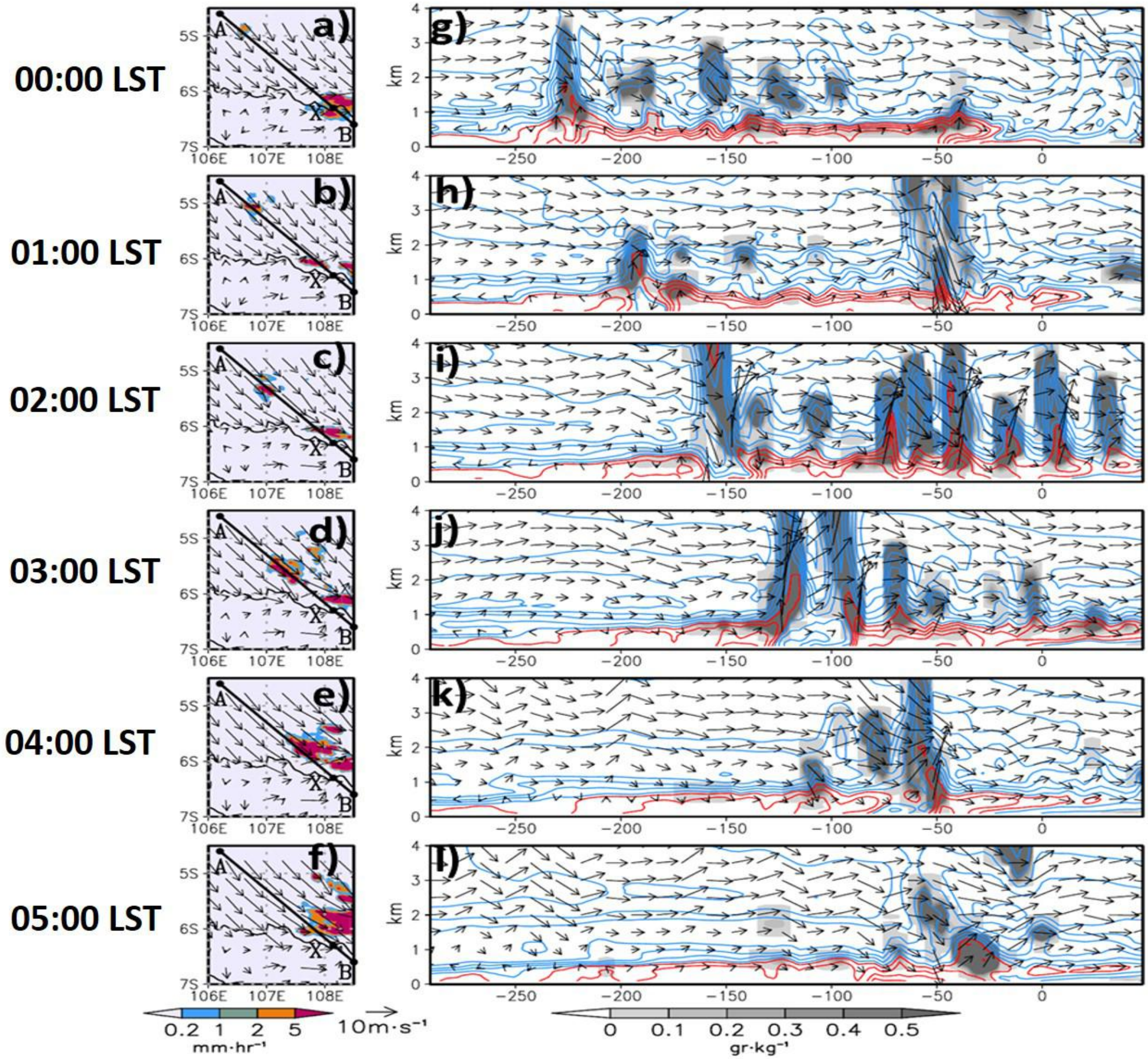


Figure 5. Time evolution of Case 1 from 00:00–05:00 LST. (a–f) Spatial pattern of hourly precipitation (shading) and 10-m horizontal winds (vectors); (g–l) vertical cross sections of winds (vectors; vertical component multiplied by 40), equivalent potential temperature (contours), and cloud mixing ratio (shading) along the thick black line from point A to point B shown in panels (a–f). The x-axis is the distance in km from point X shown in panels (a–f). For clarity, the equivalent potential temperature has had 343 K subtracted from it. Blue (red) lines indicate negative (positive) values, with a contour interval of 1.5 K starting from −0.5 K (0.5 K).

151x177mm (150 x 150 DPI)

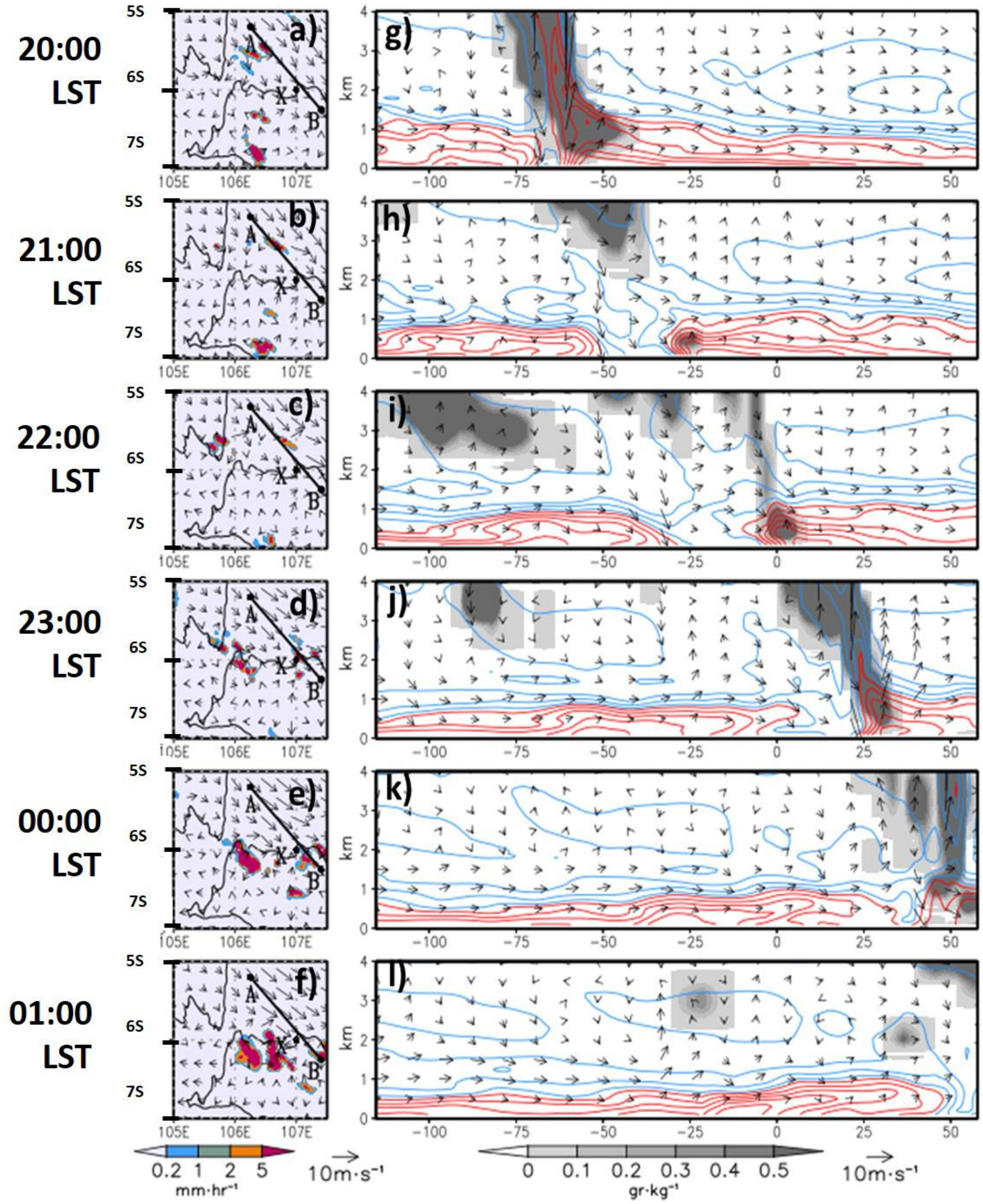


Figure 6. Same as Fig.5, but for Case 2.

180x202mm (150 x 150 DPI)

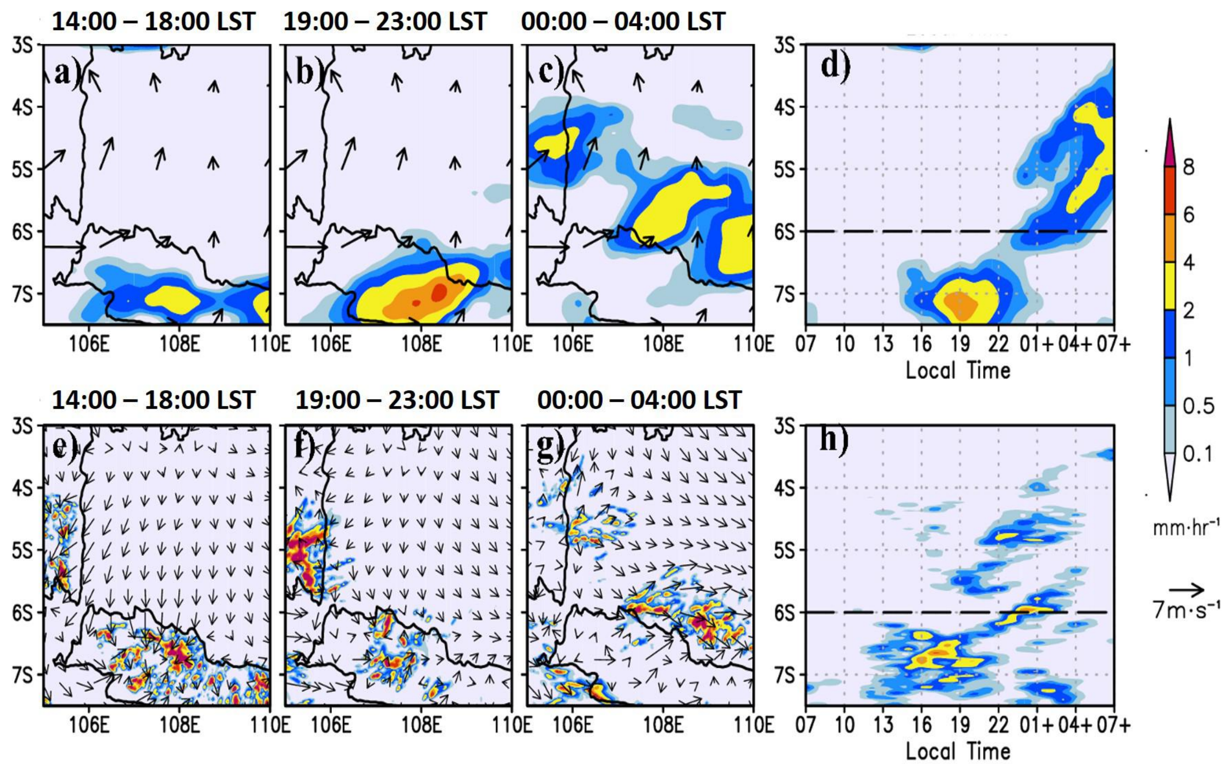


Figure 7. (a–d) Observed and (e–h) simulated features of a unique EMP event that occurred on 19 January 2012 (Case 3). Panels (a–c) and (e–g) show full spatial structures that have been averaged over the hours shown in local time at the top of the panels. Panels (d) and (h) show Hovmöller diagrams of precipitation based on the red box shown in Fig. 2. Shading denotes the rain rate. Vectors denote (a–c) the background wind field at 925 hPa and (e–g) the hourly wind field at 10 m.

170x95mm (150 x 150 DPI)

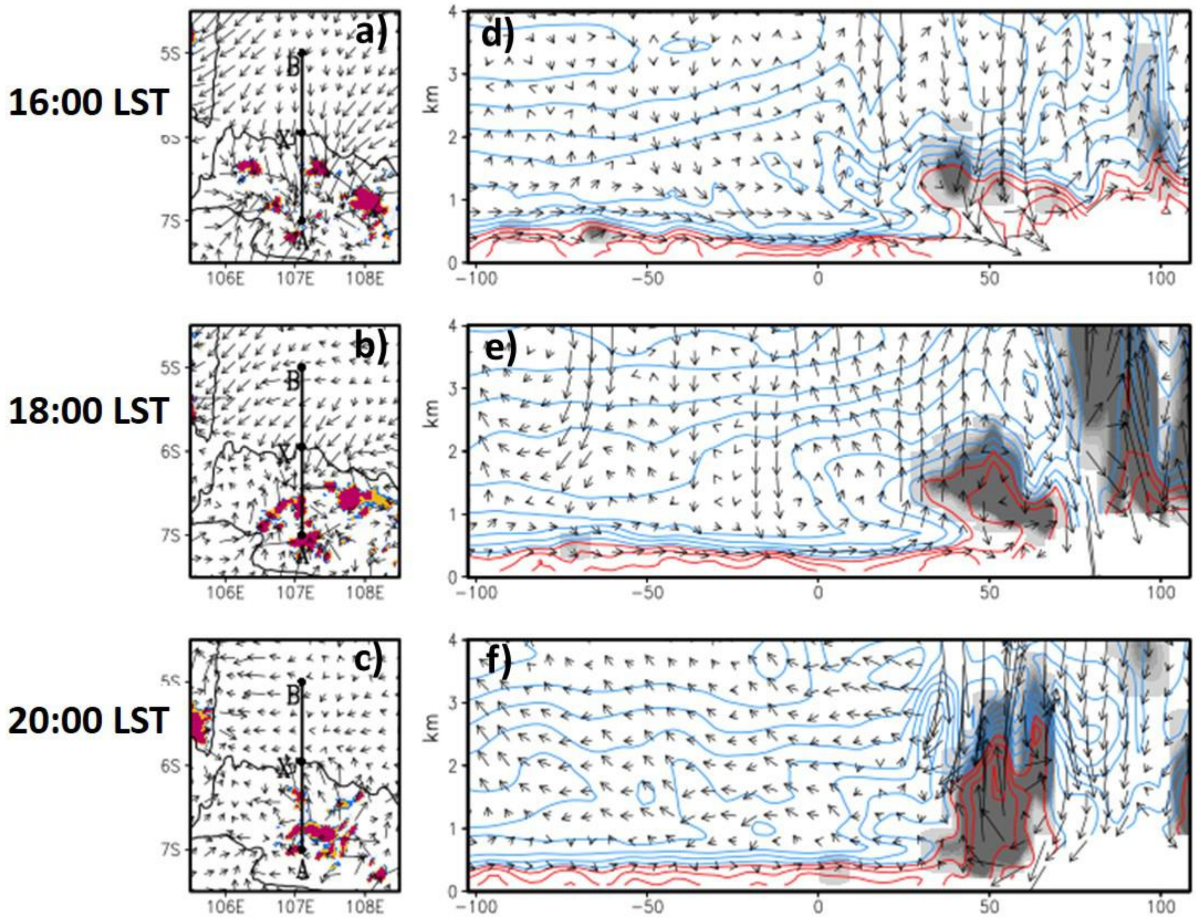


Figure 8. As in Fig. 5, but for Case 3. Spatial pattern of precipitation at: (a) 16:00 LST, (b) 18:00 LST, (c) 20:00 LST; and vertical cross sections along the thick black line from point A to point B of winds (vectors; vertical component multiplied by 40), equivalent potential temperature (contours), and cloud mixing ratio (shading) at: (d) 16:00 LST, (e) 18:00 LST, and (f) 20:00 LST.

180x149mm (150 x 150 DPI)

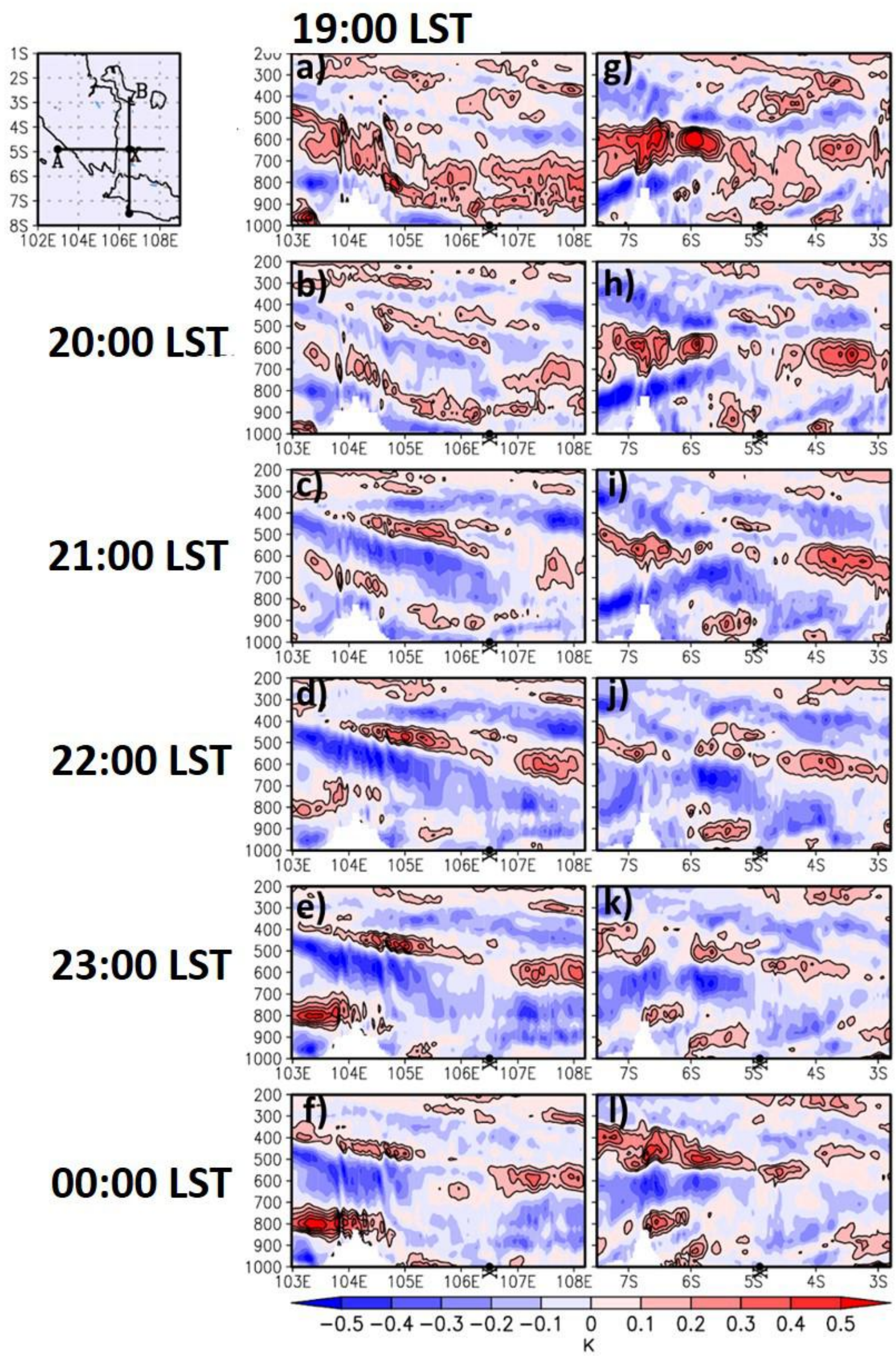


Figure 9. Vertical cross sections of potential temperature anomalies in Case 1 along (a–f) line A over 19:00–00:00 LST, and (g–l) line B over 19:00–00:00 LST. Pressure levels are given in hPa. The anomalies are constructed by subtracting the first harmonic of the diurnal cycle. Regions for lines A and B are shown in top left-hand corner.

140x211mm (150 x 150 DPI)